

# International Conference on Space Optics—ICSO 2022

Dubrovnik, Croatia

3–7 October 2022

*Edited by Kyriaki Minoglou, Nikos Karafolas, and Bruno Cugny,*



## *Light scattering from diffraction gratings*



## Light scattering from diffraction gratings

Martin Heusinger<sup>a</sup>, Marcus Trost<sup>a</sup>, Ralf Steinkopf<sup>a</sup>, Ralf Kohlhaas<sup>b</sup>, Dana Tomuta<sup>c</sup>, Roman Windpassinger<sup>c</sup>, Stefan Risse<sup>a</sup>, and Uwe Zeitner<sup>a</sup>

<sup>a</sup>Fraunhofer Institute for Applied Optics and Precision Engineering IOF,  
Albert-Einstein-Straße 7, D-07745 Jena, Germany

<sup>b</sup>SRON Netherlands Institute for Space Research, Sorbonnelaan 2, 3584 CA Utrecht, The Netherlands

<sup>c</sup>European Space Research and Technology Centre, Postbus 299, 2200 AG Noordwijk, The Netherlands

### ABSTRACT

In this contribution we will present different methods for analyzing straylight measurements in spectrometer gratings. For this purpose two different but very common types of gratings are investigated: a binary high resolution Littrow grating and a silicon-crystal echelle reflection grating. We will present several measurements and simulations on such gratings. The focus lies in particular on the difference between grating ghosts and homogeneous scattering background. It is worked out, that the homogeneous background must be evaluated by the well-established concept of "angle resolved scattering". Though, it is advantageous to use the concept of "angle resolve efficiency" for ghost analysis. Further, a simulation method is presented that allows to calculate straylight in diffraction gratings. The method is applied for ghost and background analysis and it is shown that not only the particular type of disturbance but also the grating geometry itself affects the straylight level and distribution.

**Keywords:** Optical diffraction gratings, light scattering, straylight, grating ghosts

### 1. INTRODUCTION

Nowadays, many optical applications employ diffraction gratings, which have turned into one of the most challenging components. Especially in high-performance spectrometry, the gratings, which are used as dispersive elements, are required to fulfill strong demands on the diffraction efficiency, the bandwidth, and the spectral dispersion. It has been shown that these requirements can be addressed by different grating types, e.g., binary phase gratings, echelle gratings, or blazed gratings.

Nevertheless, light scattering of such gratings becomes increasingly critical as it constrains the radiometric accuracy of spectroscopic measurements and, thus, limits the accuracy of a spectrometer. In case of spectrometer gratings, there are plenty of stray light sources due to fabrication imperfections and shape deviations of the microscopic grating structure. These deviations strongly depend on the spectrometer concept (Offner type spectrometer, echelle spectrometer, etc.) and the required grating structural feature type (e.g. binary transmission gratings, echelle type reflection gratings, blazed low-resolution gratings, etc.), respectively, and the fabrication technology (electron beam lithography, interferometry, ultra-precision diamond turning, etc.). Depending on the particular type of grating imperfection, either stochastic or more systematic and periodic light scattering effects can occur. In this sense, it is basically distinguished between a homogeneous scattering background and scattering singularities known as grating ghosts.<sup>1</sup> An analysis of these fundamentally different phenomena and their dependence on grating type, grating design, and grating fabrication will be presented. In particular, our contribution will be three-fold. It will be shown that...

---

Further author information: (Send correspondence to M. Heusinger)

M. Heusinger: E-mail: martin.heusinger@iof.fraunhofer.de, Telephone:

M. Trost: E-mail: marcus.trost@iof.fraunhofer.de, Telephone: +33 (0)1 98 76 54 32

1. ... the scattering background and grating ghosts are of different nature and should be distinguished already in light scattering measurement representation.
2. ... that scattering characteristics can already be taken into account during grating design, i.e., that for a given shape deviation, the grating structure parameters show an influence on the qualitative and quantitative scatter distribution.
3. ... that the light scattering characteristics can be controlled by the manufacturing parameters enabling a target and process optimized fabrication.

Throughout the presented analysis, different grating structural feature types will be investigated. These grating structures are chosen according to the most commonly used spectrometer types:

1. Structural feature type 1 (SFT1), Binary transmission grating for high angular dispersion:

Surface relief gratings relying on a binary corrugation of the surface of a fused silica substrate on the sub-micrometer scale are well-established components, which are already in use for current and upcoming space applications. Instruments applying binary transmission gratings are, e.g., the GAIA radial velocity spectrometer, Sentinel-4 NIR and Sentinel-5 NIR spectrometers.<sup>2,3</sup>

The geometry of a simple binary grating is described mainly by 3 parameters: grating period, groove width and grating depth whereupon the microstructure is implemented directly in the surface of a bulky glass substrate. Such gratings are typically operated in  $-1^{\text{st}}$  diffraction order in transmission under so-called Littrow condition. Depending on the desired angle of incidence (AOI), wavelength range and bandwidth, the exact grating geometry must be optimized by design. Typical key drivers for grating design are diffraction efficiency and polarization sensitivity.

In this contribution, the actual grating design is based on the FLEX/FLORIS grating.<sup>4,5</sup> With an optimization of the  $-1^{\text{st}}$  transmitted diffraction order for  $\lambda = 633 \text{ nm}$  the grating parameters amount to  $\Lambda = 667 \text{ nm}$  and  $AOI = 23.8^\circ$ .

Within this work, the SFT1-grating is fabricated by a combination of electron beam lithography (EBL) and dry etching processes (reactive ion etching, RIE).

2. SFT2, Echelle type reflection grating in silicon using wet-anisotropic etching:

A second type of surface relief gratings are echelle or echelette gratings, where the special focus lies on silicon as substrate material. Echelle gratings are typically operated in reflection and in some higher diffraction order considerably larger than one. Using silicon as substrate material is especially attractive for infrared applications, where an operation in immersion increases the resolution of grating spectrometers significantly.<sup>3</sup> Typical periods for such gratings extend from  $\approx 1 \mu\text{m}$  up to several tenth of micrometers. Already running missions or instruments that use silicon immersed gratings are, e.g., the SWIR-channels of the spectrometer of the Sentinel-5 and Sentinel-5P instruments. The basic micro-structure of silicon echelle gratings is depicted in Figure 1(b). Most notably, the characteristic angles  $\alpha$  and  $\beta$  are solely defined by the crystallographic orientation of the silicon crystal. These angles can be continuously adjusted by preparing the surface orientation of the underlying silicon crystal, i.e., the angle  $\gamma$ .

For the investigations presented in this paper, the grating is desgin according to the Sentinel-5 SW2-grating,<sup>3</sup> i.e.,  $\Lambda = 2070 \mu\text{m}$ ,  $\gamma = 0^\circ$ . Despite the fact, that immersed gratings are a very important application scenario, the investigations presented in this paper focus on the analysis and optimization of the actual grating's micro-structure. Thus, standard silicon wafers are used as substrate material (without bonding to a prism) and all optical measurements and performance analysis are considered to be performed in direct reflection with light impinging from air onto the corrugated surface.

## 2. ANALYSIS OF STRAYLIGHT MEASUREMENTS

The angle resolved scattering ARS is usually measured by focussing the illuminating beam onto an aperture (slit or pinhole) in front of the detector.<sup>6</sup> The light source and the detector are mounted onto a goniometer, which

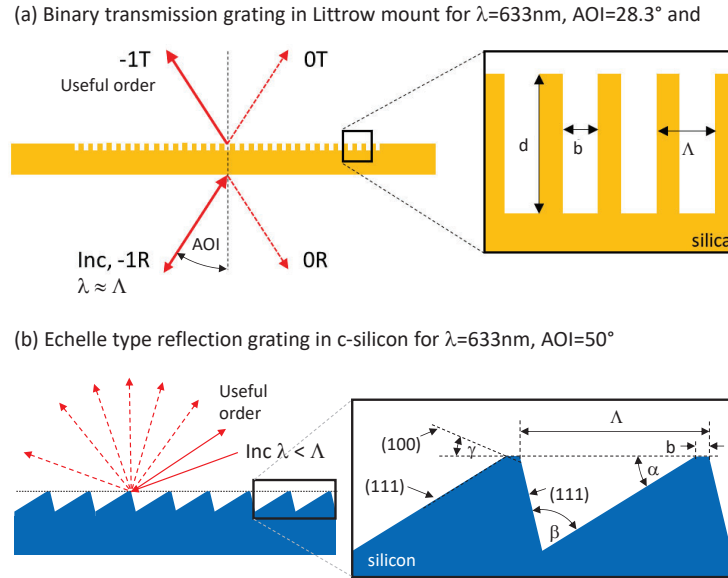


Figure 1. Illustration of the grating structures considered within this work: (a) binary transmission grating used in Littrow mount with  $\Lambda = 667$  nm,  $AOI = 23.8^\circ$ ,  $\lambda = 633$  nm, (b) echelle grating with  $\Lambda = 2070$  nm,  $AOI = 55^\circ$ ,  $\lambda = 633$  nm.

allows to scan the full scattering half space defined by the azimuthal angle  $\theta$  and conical angle  $\varphi$ . The ARS is then calculated by

$$ARS(\theta, \varphi) = \frac{P_S(\theta, \varphi)}{P_0 \Omega} = \frac{ARE(\theta, \varphi)}{\Omega}, \quad (1)$$

with  $P_S$  being the signal power measured by the detector,  $P_0$  the power of the incident beam and  $\Omega$  the aperture angle, which is in particular determined by the pinhole size.

In order to illustrate the impact of different set-up configurations, several ARS measurements with different aperture angles  $\Omega$  were performed. The measurements were done on a SFT2-grating according to the configuration as described in Fig. 1b, i.e.,  $AOI = 55^\circ$ ,  $\lambda = 633$  nm,  $\Lambda = 2070$  nm. The measurement results are shown in Figure 2. In the applied configuration, the grating shows 5 propagating diffraction orders in reflection half space, which can be clearly identified. In Figure 2a three main properties can be identified: First, a homogeneous straylight background especially rising around the  $-5^{\text{th}}$  DO (useful order) is detected. Second, the dispersion plane (defined by  $\varphi = 0^\circ$  and  $\theta = -90^\circ \dots 90^\circ$ ) shows an increased straylight level. Third, along dispersion plane and in between the main diffraction orders, several grating ghosts are slightly visible.

Figure 2b shows the ARS-measurements along dispersion plane around the  $-5^{\text{th}}$  DO. The measurements have been performed with an oversampling, i.e., with a step width of only  $0.02^\circ$ , in order to ensure a full detection of the ghosts. The grating ghosts can now be clearly identified as they are rising out of a continuous scattering background. It is further clearly visible that the scattering background is always detected on the same level and, thus, is independent of the measurement set-up. Though, the strength of the grating ghosts strongly depends on the aperture angle; they are the stronger, the smaller the aperture angle. This becomes clear when considering the ghosts as spurious diffraction orders that arise from a super-period in the diffraction grating [RefHeusinger]: In this sense, the measured signal power of the ghost and the ghost efficiency  $\eta_S$ , respectively, should be independent of  $\Omega$  as long as the ghost is fully detected (meaning that the aperture must be big enough to allow measuring the full ghost). The corresponding measurement will be referred to as “angle resolved efficiency” (ARE) measurement, which simply can be derived from the ARS measurements by  $ARE = ARS \cdot \Omega$ . Though, oversampling and a suited aperture has to be ensured.

The corresponding ARE of the SFT2 test grating is shown in Figure 2c. The Figure contains several comments, which explain the features visible in the measurement. Regarding the ghost characterization, we find that the

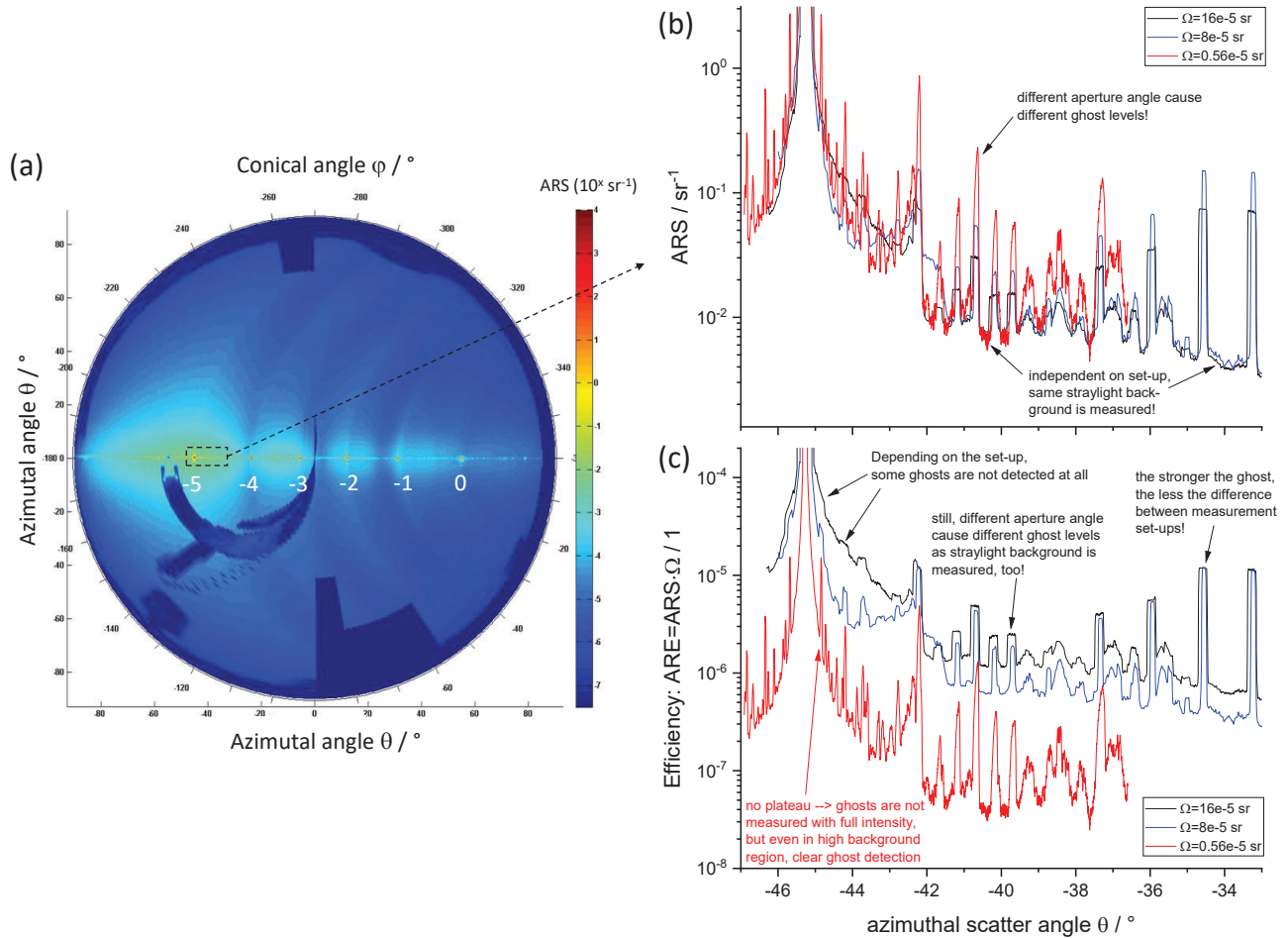


Figure 2. Analysis of different straylight measurements (different aperture angles  $\Omega$ ) of a holographically fabricated SFT2 test grating measured according to Figure 1(b): (a) 3D-ARS-measurement of the full transmission half space. (b) ARS-measurements with different aperture angle  $\Omega$  along the dispersion plane around the  $-5^{\text{th}}$  DO for  $\varphi = 0^\circ$  and  $\theta = -47^\circ \dots -33^\circ$ . (c) Very same measurements as in (b), but in efficiency representation, i.e., angle resolved efficiency measurement  $ARE = ARS \cdot \Omega$ .

strength of the ghosts is in the range  $ARE < 10^{-4}$  with the strongest ghost in close vicinity to the  $-5^{\text{th}}$  DO.

### 3. THEORETICAL ANALYSIS OF SCATTERED LIGHT DISTRIBUTION

#### 3.1 Basic model for straylight simulation

For simulating the light propagation and eventually the intensity distribution in the half-space of a transmission grating we used the *rigorous coupled wave analysis* (RCWA).<sup>7</sup> This algorithm numerically calculates the light propagation of an electromagnetic plane wave incident upon a periodically structured surface with period  $\Lambda$  and in particular the diffraction efficiency of the propagating diffraction orders. E.g., the ideal SFT1-grating (period  $p = 667 \text{ nm}$ , incidence angle  $AOI = 23.8^\circ$  in air and wavelength  $\lambda = 633 \text{ nm}$ ) possesses only 2 diffraction orders in transmission half space.

Scattered light is now caused by large scale variations of the ideal grating structure with typical length scales  $P \gg \Lambda$ . In order to simulate the intensity distribution of the diffusely scattered light we still use RCWA by introducing a super-lattice with period  $P = N_p \cdot \Lambda$ . Such a compound of many single periods  $\Lambda$  possesses additional diffraction orders. For example, in case of the SFT1-grating there are 8 propagating orders for  $N_p = 4$ .

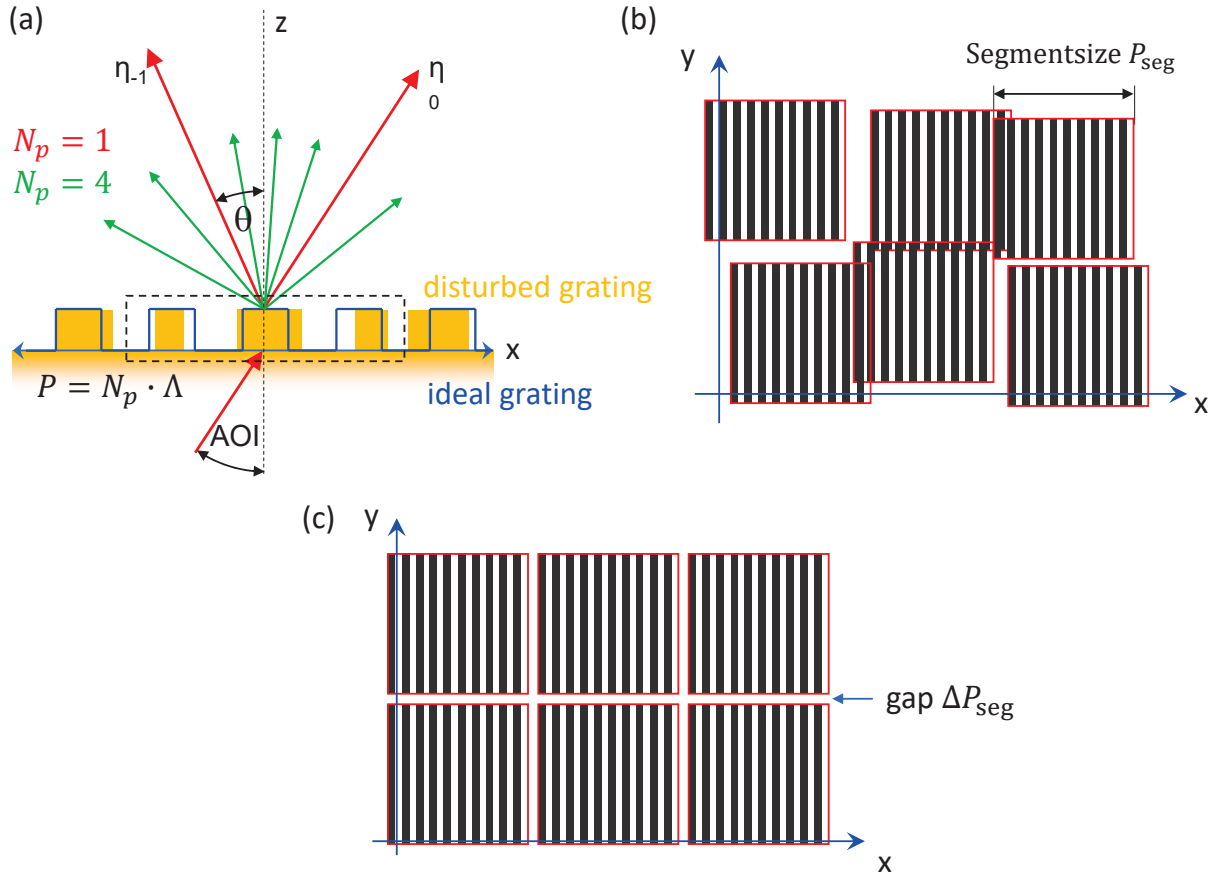


Figure 3. RCWA simulation approach for simulating straylight of disturbed gratings. A super lattice with extent  $P = N_p \cdot \Lambda$  is introduced, which allows to consider gratings with local geometrical disturbances of their mikrostructure (a) and illustration of the stochastic (b) and deterministic (c) segment alignment error ("stitching error") occurring in sequential writing processes.

The effect of increasing  $P$  is depicted in Fig. 3a. More and more diffraction orders appear and in the limit of  $N \rightarrow \infty$  we end up with a quasi-continuous scattering background. Here, we will denote the additional diffraction orders as *straylight orders* (SO). In the case of an ideal undisturbed grating, the SOs have an intensity of zero and thus give the same result as  $N_p = 1$ . However, a disturbance of the ideal grating geometry results in a certain amount of energy in every SO. The diffraction efficiency  $\eta_m(\theta_m)$  is calculated by the RCWA algorithm and the angle resolved scattering<sup>6</sup> (ARS) can be estimated by

$$ARS_{1D}(\theta_m) \approx \frac{\eta_m}{\frac{\theta_{m-1} + \theta_m}{2} - \frac{\theta_{m+1} + \theta_m}{2}}. \quad (2)$$

The corresponding scattering angle  $\theta_m$  is calculated using the grating equation

$$\theta_m = \arcsin \left( \sin \theta_i + \frac{m\lambda}{N_p} \right) \quad (3)$$

with  $m = m_{min}, \dots, m_{max}$  enumerating the propagating straylight and diffraction orders. More details of this model and the extend to 2D-disturbances can be found in.<sup>8</sup>

### 3.2 Simulating ghosts

In case of SFT1 and also SFT2, we apply electron beam lithography and in particular the "variable-shaped-beam" approach (VSB) for defining the mikrostructure. Within this method, the broadened electron beam is

shaped by means of two rectangular apertures (this shaped beam is called a "Shot" with adjustable dimensions of maximum  $2.5 \mu\text{m} \times 2.5 \mu\text{m}$ ). The precise position of the *Shot* on the sample is controlled by different electromagnetic deflection systems in the electron column. Additionally, the substrate to be exposed is mounted on a substrate stage moving along x- and y-direction. The different positioning systems generate grating sub-segments with size  $P_{\text{seg}} \gg \Lambda$ , which are stitched together to the final full size grating. An imperfect alignment of these segments causes the super-periods and eventually the grating ghosts.

Within this work, we simulate the effects of, first, a stochastic alignment error (AE)  $\sigma_{\text{seg}}$  of the sub-segments and, second, a deterministic alignment error  $\Delta P_{\text{seg}}$  resulting in a gap ( $\Delta P_{\text{seg}} > 0$ ) or overlay ( $\Delta P_{\text{seg}} < 0$ ) between adjacent sub-segments. The effect of this error is calculated for a sub-segment size of  $P_{\text{seg}} \approx 35 \mu\text{m}$  as it occurs in the used e-beam writer. Figure 4 shows the results of the simulation.

The main findings from the simulation are the following:

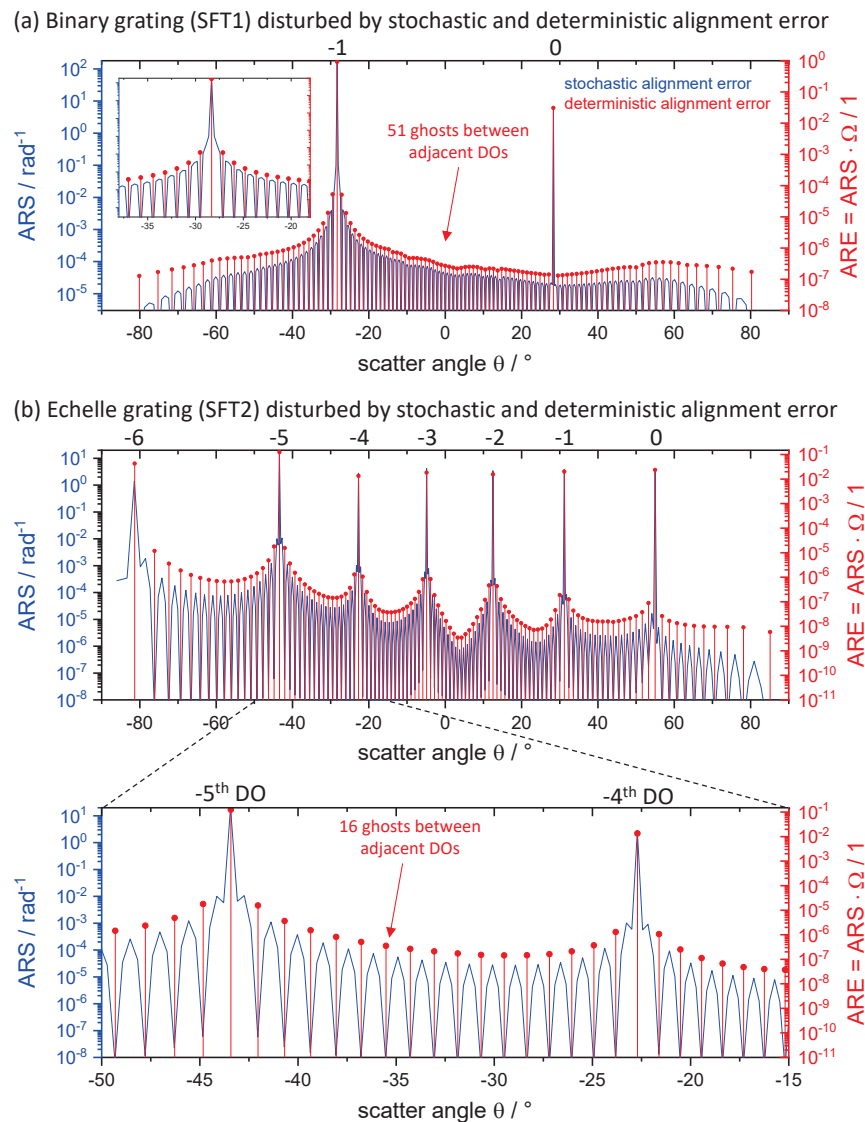


Figure 4. Effect of a deterministic and systematic positioning/alignment error occurring in sequential fabrication technologies (such as EBL) for the SFT1 and SFT2 grating type. The sub-segment size is  $P_{\text{seg}} = 35 \mu\text{m} \approx 52 \cdot \Lambda_{\text{SFT1}} \approx 17 \cdot \Lambda_{\text{SFT2}}$  and the alignment errors have the strength  $\sigma = 5 \text{ nm}$  and  $\Delta P_{\text{seg}} = 5 \text{ nm}$ .

1. The stochastic AE doesn't generate grating ghosts at all! Instead, a homogeneous straylight background occurs showing sharp dips (local minima) exactly where we would expect the grating ghosts.
2. The deterministic AE generates grating ghosts exactly at the expected angular positions.
3. Beside these differences, both, stochastic and deterministic AE behave qualitatively very similar along the whole dispersion plane. The ghosts generated by the deterministic AE are exactly in the minima generated by the stochastic AE. The strength of the straylight (either ghosts or background with minima) becomes stronger in vicinity to the main diffraction orders of the grating. Especially the useful diffraction order ( $-1^{\text{st}}$  DO for SFT1 and  $-5^{\text{th}}$  DO for SFT2) is surrounded by the strongest straylight artefacts.
4. There is basically no difference between the straylight generated in the SFT1 and SFT2 grating regarding both, the total number and position of the ghosts and the strength of the ghosts. Due to a sub-segment size of  $P_{\text{seg}} = 35 \mu\text{m} \approx 52 \cdot \Lambda_{\text{SFT1}} \approx 17 \cdot \Lambda_{\text{SFT2}}$ , the SFT1-grating shows 51 ghosts between adjacent diffraction orders while the SFT2-grating shows only 16 ghosts between adjacent DOs.
5. The strength of the straylight patterns are related to the strength of the disturbance  $\sigma_{\text{seg}}$  and  $\Delta P_{\text{seg}}$ , respectively. However, the distribution of the straylight (i.e., the qualitative behaviour) is not affected by the disturbance strength. This is not shown in Fig. 4.

### 3.3 Simulating background

The fabrication of the SFT1- and SFT2-grating by EBL also results in slight local errors of the *Shot* positioning and *Shot* format, which results in a locally varying grating period and groove width. The straylight simulation can account for these fabrication error by introducing the parameter  $\sigma_p$  describing the *Shot* positioning error and  $\sigma_b$  describing the stochastic error of the groove width. In the following, the effect of these errors onto the straylight spectrum is presented.

#### 3.3.1 Binary high resolution grating

It is commonly known that binary gratings (with periods in the range of the wavelength) illuminated in Littrow mount show very high diffraction efficiencies in the  $-1^{\text{st}}$  diffraction order for various combinations of grating depth  $d$  and dutycycle  $\text{FF} = \frac{\Lambda-b}{\Lambda}$ .<sup>9,10</sup> E.g., For TE-polarized light the dependency  $\eta_{-1}(d, \text{FF})$  of the investigated SFT1-grating ( $p = 667 \text{ nm}$ ,  $\lambda = 633 \text{ nm}$ ,  $\theta_i = 28.3^\circ$ ) is shown in Fig. 5a. The figure reveals that there are several possible grating designs that allow diffraction efficiencies of more than 90%. The presented straylight

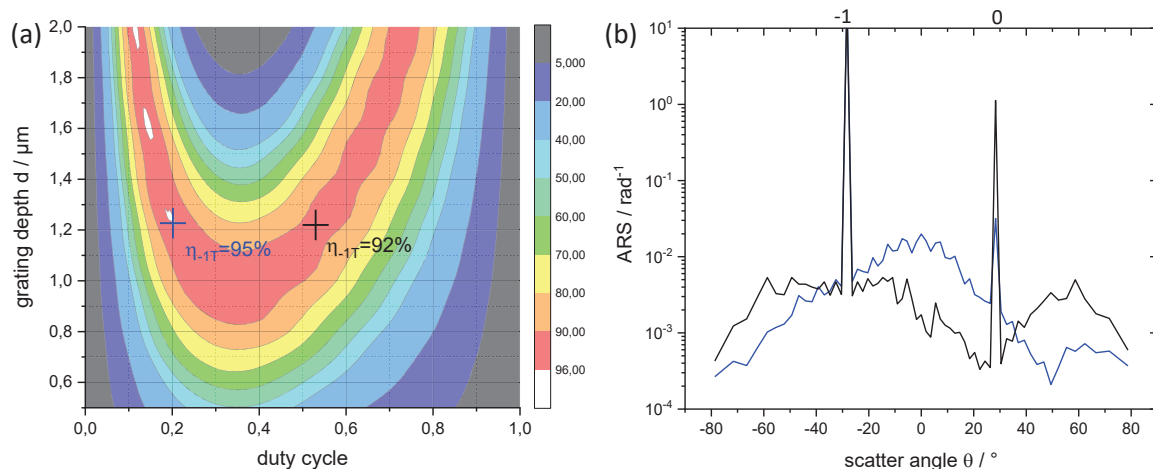


Figure 5. (a) Efficiency of the  $-1^{\text{st}}$  DO of the SFT1-grating dependent on the grating depth  $d$  and the dutycycle FF (for  $\lambda = 633 \text{ nm}$ ,  $\text{AOI} = 23.8^\circ$  (in air) and TE-polarization). (b) Straylight simulations for very different FF and constant  $d$  with maximum  $\eta_{-1}$  (marks in (a)).

simulation method allows for investigating the straylight performance depending on the grating geometry and, hence, to consider straylight specifications already in the grating design process. For this purpose, the scattering spectra for two different possible grating geometries with maximum  $\eta_{-1}$  and specified *Shot* inaccuracies defined by  $\sigma_p = 5$  nm, and  $\sigma_b = 5$  nm are evaluated.

Figure 5b shows the scattered light distribution of gratings with different dutycycle  $FF = 0.2$  and  $FF = 0.53$ , but constant depth  $d = 1220$  nm (marks in Fig. 5a). The corresponding straylight spectra (Fig. 5c) show a very different angular distribution along dispersion plane. Whereas the curve for  $FF = 0.2$  possesses a very high straylight level in particular between the  $-1^{\text{st}}$  and  $0^{\text{th}}$  DO ( $\theta = [-23.8^\circ, \dots, 23.8^\circ]$ ) and decreases by two orders of magnitude for higher scattering angles, the grating with  $FF = 0.53$  shows basically the reverse behaviour. There, we find a weak straylight level in the angular range between the main diffraction orders and especially around the  $0^{\text{th}}$  DO.

This investigation shows, that the grating geometry and the grating design, respectively, have an influence onto the straylight distribution. With the simple presented simulation method it is possible to evaluate the straylight generated by a certain grating structure already during design process.

### 3.3.2 Echelle grating

The same simulation principle can be applied for the presented SFT2-grating. The grating geometry of this grating type is predetermined by the grating period  $\Lambda$  and the crystallographic structure of the silicon substrate. Therefore, there are no degrees of freedom in the grating geometry as there are for the SFT1 grating (depth and dutycycle as investigated in Sec. 3.3.1). However, a straylight simulation for the fixed geometry can be compared to a straylight measurement in order to evaluate the error of the line positioning  $\sigma_p$  and the error of the line width  $\sigma_b$ . Such an investigation is shown in Figure 6.

Measurement and simulation fit very well: even the local minima within the continuous straylight background are met by the simulation. Though, the absolute straylight level around the  $-5^{\text{th}}$  DO differs slightly. Further, the simulation curve of course does not possess ghosts as no deterministic errors were considered within the applied simulation. The measured ghosts show an unexpected distribution as they are the strongest in middle of adjacent

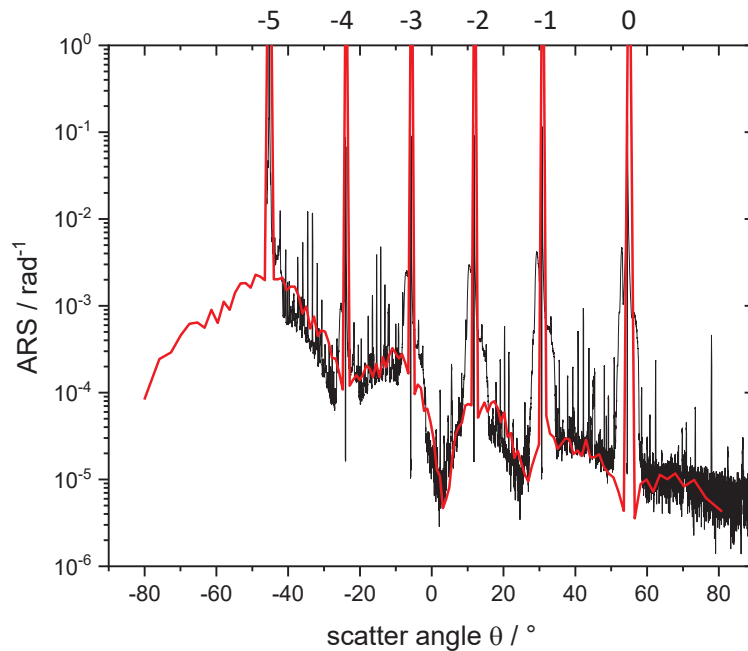


Figure 6. Straylight simulation along the dispersion plane (i.e.  $\varphi = 0^\circ$ ) of the SFT2-grating (echelle type grating in reflexion with  $\Lambda = 2070$  nm,  $AOI = 55^\circ$ ,  $\lambda = 633$  nm according to Fig. 1b) disturbed by a stochastic line position error  $\sigma_p = 0.4$  nm and line width error  $\sigma_b = 0.4$  nm (red curve) compared with a straylight measurement of the very same test grating as presented in Fig. 2 (black curve).

DOs. As explained in Sec. 3.2, an increase close to the main diffraction orders would be expected. The reason is probably a different formation of super periods during holography, which was applied for the investigated test grating. The mechanisms responsible for super period formation that finally leads to ghosts as observed in Fig. 6 is still unknown and under investigation.

## 4. GRATING FABRICATION

### 4.1 BINARY HIGH RESOLUTION GRATING

One approach to reduce the straylight level and especially to lower the Rowland ghosts is the direct improvement of the positioning accuracy in the EBL writing process, i.e. the improvement of the stitching of the single sub-segments. In this investigation we aim for controlling the gap between adjacent segments as illustrated in Fig. 3c. The e-beam-writer offers several calibration parameters that control the segment alignment. The calibration of the *micro deflection system* and in this way the gap  $\Delta P_{\text{seg}}$  is controlled by the parameter  $\Delta\text{MDS}$ . An experiment was performed, in which several grating with different  $\Delta\text{MDS}$  were fabricated and the corresponding straylight performance around the  $-1^{\text{st}}$  DO was measured. The measurement result of the best and worst calibration state is shown in Fig. 7a. The blue arrows in this graph mark the expected angular positions of the ghosts that

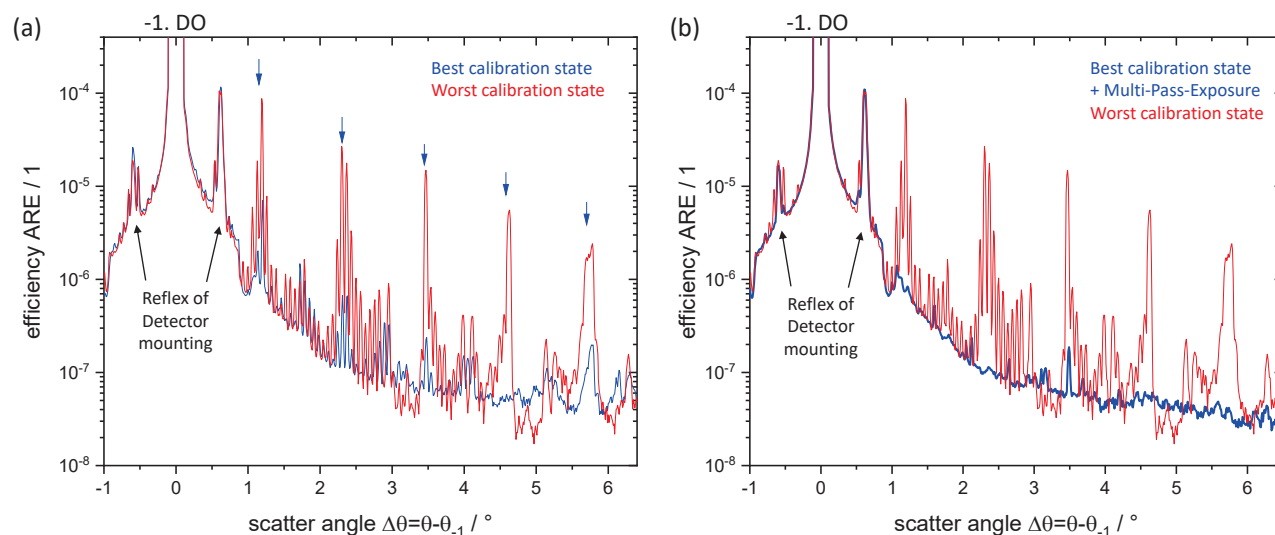


Figure 7. Straylight measurement of the grating ghosts around the  $-1^{\text{st}}$  DO (at  $\Delta\theta = 0^\circ$ ) of the SFT1-grating with the blue arrows marking the calculated angular positions of the ghosts corresponding to the “*micro deflection system*” (segment size of  $P_{\text{seg}} = 35 \mu\text{m}$ ): (a) Straylight curves of the best and worst calibration state. (b) Additionally applied Multipass-exposure for further improvement of the best calibration state.

correspond to the applied segment size of  $P_{\text{seg}} = 35 \mu\text{m}$ . In the graph, there occur a lot of weaker ghosts that correspond to second deflection system (“*macro deflection system*”), which is not investigated here. However, as we see in Fig. 7a, the calibration of the *micro deflection system* strongly affects the strength of the corresponding peaks, but also reduces the strength of the ghosts originating from the *macro deflection system*. Further, we applied a so-called *multi-pass exposure*<sup>11</sup> that allows to reduce the ghosts further as shown in Fig. 7b.

### 4.2 ECHELLE GRATING

The fabrication of echelle gratings in a silicon crystal substrate applies two crucial steps. First, the realization of the lateral grating pattern into a grating hard mask (usually chromium or silicon nitride) by means of a suited lithography process, e.g., holography or electron beam lithography. Within this work, we use EBL for lateral structuring. Second, the transfer of the lateral structure into the silicon crystal by wet anisotropic etching. The second step is done by KOH-etching of the [100]-cSi-substrate, which inherently leads to the formation of the desired echelle profile according to the crystallographic planes of the Si-crystal. During the second step, a correct

alignment of the grating lines with respect to the crystal orientation is mandatory. The alignment can either be realized by a rotation of the grating pattern during EBL-data preparation or by rotation of the substrate during lithography.

Within this work, the effect of different rotation methods onto the straylight pattern was tested:

1. Tilting of the EBL exposure pattern in the standard EBL-exposure regime. This leads to a step-like pattern in the latent exposure profile, which might slightly be transferred into the resist and hard mask pattern, respectively.
2. Tilting of the EBL exposure pattern with randomly overlapping Shots in a multipass exposure regime with the intention to reduce the artifacts generated by the steps within the latent exposure pattern.
3. Standard EBL exposure pattern (without tilting) and rotation of the substrate, which completely avoids steps within the exposure pattern.

The straylight measurements of the full transmission hemisphere according to Fig. 1b and an SEM-image of the grating profile inspection is shown in Fig. 8.

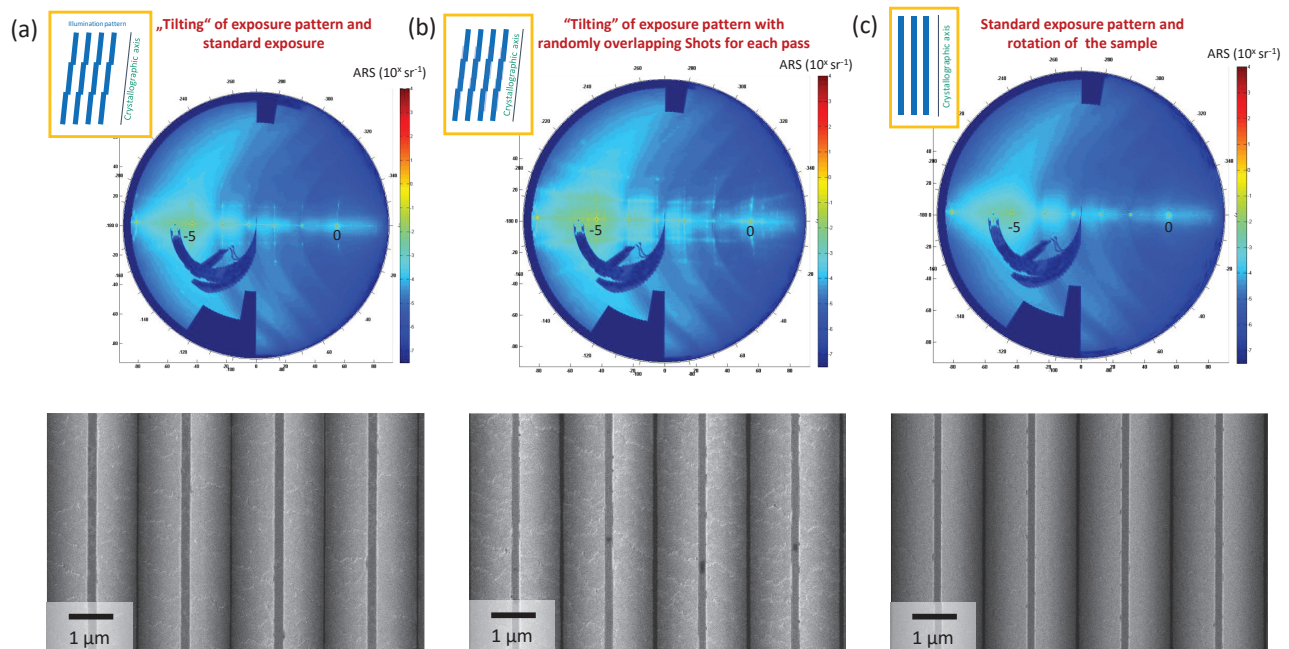


Figure 8. *Top*: Full ARS measurements of the complete reflection hemisphere of the SFT2 grating (echelle type grating in reflexion with  $\Lambda = 2070$  nm,  $\text{AOI} = 55^\circ$ ,  $\lambda = 633$  nm according to Fig. 1b). The dark blue region obscuration of the light source. *Bottom*: Corresponding SEM-images of the grating structure.

It is clearly found that the third method produces the lowest straylight level. The first two methods produce grating ghosts within the whole half space. The ghosts of grating 1 (standard tilting) are more pronounced than the ghosts of grating 2, which are rather blurred. However, the total straylight level of grating 2 and especially the straylight background is considerably higher. This can also be confirmed by SEM-inspection of the grating structure. Grating 2 shows a significantly increased facet roughness. The facet roughness of grating 3 is almost not visible within the SEM image.

## 5. CONCLUSION

The conclusion is three-fold as is the total paper:

First, it was shown that homogeneous straylight background and grating ghosts of significant difference as the

background is a continuous effect while the ghosts are singularities. As such, the background must be evaluated in terms of ARS-measurements while the ghosts need to be evaluated in terms of efficiency measurements. Within the paper we used the term "angle resolved efficiency" for such a measurement as it is closely related to ARS. Second, a simulation method is presented that allows to calculate straylight in diffraction gratings. The method is applied for ghost and background analysis and it is shown that not only the particular type of disturbance but also the grating geometry itself affects the straylight level and distribution. A comparison of ARS-measurement and ARS-simulation verifies the model.

Third, investigations on straylight optimization in binary transmission gratings and echelle reflection gratings are presented. By means of calibrating the deflection system of the applied e-beam writer a reduction of the grating ghosts by more than 2 orders of magnitude was achieved.

## ACKNOWLEDGMENTS

This work was funded by the European Space Agency (ESA) and the European Space Research and Technology Centre (ESTEC).

## REFERENCES

- [1] Palmer, C. A., Loewen, E. G., and Thermo, R., [*Diffraction grating handbook*], Newport Corporation Springfield, Ohio, USA (2005).
- [2] Erdmann, M., Kley, E.-B., and Zeitner, U., "Development of a large blazed transmission grating by effective binary index modulation for the gaia radial velocity spectrometer," in [*International Conference on Space Optics—ICSO 2010*], **10565**, 373–378, SPIE (2017).
- [3] Kohlhaas, R., Tol, P., Schuurhof, R., Huisman, R., Yates, S. J., Keizer, G., Wanders, R., van Loon, S., Coppens, T., Kaykisiz, M., et al., "Manufacturing and optical performance of silicon immersed gratings for sentinel-5," in [*International Conference on Space Optics—ICSO 2018*], **11180**, 585–605, SPIE (2019).
- [4] Kraft, S., Bézy, J.-L., Del Bello, U., Berlich, R., Drusch, M., Franco, R., Gabriele, A., Harnisch, B., Meynart, R., and Silvestrin, P., "Floris: Phase a status of the fluorescence imaging spectrometer of the earth explorer mission candidate flex," in [*SPIE Remote Sensing*], 88890T–88890T, International Society for Optics and Photonics (2013).
- [5] Kraft, S., Del Bello, U., Harnisch, B., Bouvet, M., Drusch, M., and Bézy, J.-L., "Fluorescence imaging spectrometer concepts for the earth explorer mission candidate flex," in [*International Conference on Space Optics—ICSO 2012*], **10564**, 105641W, International Society for Optics and Photonics (2017).
- [6] Schröder, S., Duparré, A., Coriand, L., Tünnermann, A., Penalver, D. H., and Harvey, J. E., "Modeling of light scattering in different regimes of surface roughness," *Optics express* **19**(10), 9820–9835 (2011).
- [7] Moharam, M., Gaylord, T., Grann, E. B., and Pommet, D. A., "Formulation for stable and efficient implementation of the rigorous coupled-wave analysis of binary gratings," *JOSA A* **12**(5), 1068–1076 (1995).
- [8] Heusinger, M., Michaelis, D., Flügel-Paul, T., and Zeitner, U. D., "Diffuse scattering due to stochastic disturbances of 1d-gratings on the example of line edge roughness," *Optics Express* **26**(21), 28104–28118 (2018).
- [9] Nguyen, H., Shore, B., Bryan, S., Britten, J., Boyd, R., and Perry, M., "High-efficiency fused-silica transmission gratings," *Optics letters* **22**(3), 142–144 (1997).
- [10] Clausnitzer, T., Kley, E.-B., Fuchs, H.-J., and Tuennermann, A., "Highly efficient polarization-independent transmission gratings for pulse stretching and compression," in [*Optical Fabrication, Testing, and Metrology*], **5252**, 174–183, International Society for Optics and Photonics (2004).
- [11] Berglund, C. N., Thomas, J. R., and Poreda, J. T., "Multiphase printing for e-beam lithography," (Apr. 7 1992). US Patent 5,103,101.